Flux Maps Spatial Harmonic Modeling and Measurement in Synchronous Reluctance Motors

Flux Maps Spatial Harmonic Modeling and Measurement in Synchronous Reluctance Motors

Anantaram Varatharajan
Dipartimento Energia Galileo Ferraris
Politecnico di Torino
Turin, Italy
varatharajan@ieee.org

Paolo Pescetto
Dipartimento Energia Galileo Ferraris
Politecnico di Torino
Turin, Italy
paolo.pescetto@polito.it

Simone Ferrari
Dipartimento Energia Galileo Ferraris
Politecnico di Torino
Turin, Italy
simone.ferrari@polito.it

Gianmario Pellegrino
Dipartimento Energia Galileo Ferraris
Politecnico di Torino
Turin, Italy
gianmario.pellegrino@polito.it

***Abstract*—This work proposes a novel identification test and post-processing procedure to measure the complete flux linkage model of a synchronous reluctance (SyR) machine, including its spatial harmonics. A novel space harmonic flux model is developed, capable of describing the machine behavior even under distorted current waveforms. This permits to characterize the machine by adopting standard and straightforward PI-based current vector control, avoiding the use of the resonant controllers normally adopted in similar tests procedures present in the literature. The flux ripple information is extracted by combining the space distortion in the stator current and voltage. The flux ripple measurement can be used for validating the FEA model of the SyR machine, thus improving the motor design stage, for experimentally estimating the motor torque ripple and for building accurate simulation models including the space harmonics. this is particularly critical for very low-speed applications, accurate position control, and sensorless drives. An experimental validation is carried out on a 4.4 kW SyR machine.**

***Index Terms*—Synchronous Reluctance Motor, Space harmonics, Flux maps identification, Magnetic saturation**

I. Introduction

In the last decade, the synchronous motor drives are progressively replacing the traditional grid connected induction motors in a growing number of applications. In particular, the Synchronous Reluctance Motors (SyRMs) are an attractive solution for many industrial drives thanks to their low manufacturing cost and high efficiency. Anyway, most of the synchronous machines, and especially the high anisotropy ones like the SyRMs, exhibit highly nonlinear magnetic saturation characteristics, also called flux maps, due to saturation and cross-saturation phenomena. In addition, for many synchronous motors designed for low cost applications the space harmonic distortion in the flux linkage characteristic is relevant.

In this scenario, an advanced modeling of the electrical machines is imperative, both for the design and control purposes, where the flux linkages are dependent not only on the stator current, but also on the rotor position, as indicated in Figure 1. The motor design stage is often assisted by Finite Element Analysis (FEA), which include the motor saturation characteristic and its space harmonics, but require to be calibrated and validated through experimental testing. On the control side, accurate knowledge of the flux maps is a key requirement for several model-based techniques, for evaluating the optimal control trajectories, such as MTPA and MTPV [1], [2], for ensuring the stability of many sensorless control strategies [3]–[6] and for building accurate simulation models of the drive [7].

Normally, the experimental identification of the flux maps of synchronous motors [8]–[13] only considers its fundamental components, leading to a two-dimensional (2D) representation with the stator fluxes $\lambda_d(i_d, i_q)$, $\lambda_q(i_d, i_q)$, function of the i_d and i_q currents. However, the spatial flux harmonics may affect the motor control stability, especially at low-speed. This is particularly critical in sensorless applications, where High Frequency (HF) signal injection is normally adopted for position estimate [14]–[17]. Thus, an instantaneous $dq\theta$ flux-map is mandatory, where the flux linkages are expressed as three-dimensional (3D) quantities, $\lambda_d(i_d, i_q, \theta)$, $\lambda_q(i_d, i_q, \theta)$, function of the dq currents and the rotor position θ [18].

The advanced magnetic models found in the literature, and including the flux harmonics effects, are normally based on the assumption of sinusoidal phase current or voltage. For this reason, the experimental measurement of the flux spatial harmonics is not trivial. Existing procedures [19], [20] use

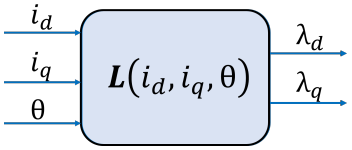

Fig. 1. Concept of $dq\theta$ flux maps to include the space harmonic effects.

the discrete Fourier transform (DFT) to extract the harmonics. The method requires perfectly sinusoidal phase current during the test, retrieving the flux space harmonics from the corresponding undulation in the back-EMF. In order to obtain sinusoidal phase current, dedicated PI-resonant (PIR) current controllers are adopted for each harmonic order. However, this requires a preliminary knowledge of the relevant flux harmonics orders. Moreover, the feasibility of PIR controller for machines with higher dominant harmonic order (e.g. 18^{th}, 24^{th}) is challenging and depends on the operating speed and sampling frequency.

To overcome these issues, this work proposes a new spatial harmonic model and identification test. The novel magnetic model is capable of describing the fundamental and harmonic flux characteristic even under non-sinusoidal phase current. Therefore, simple PI current controllers with coarse preliminary calibration can be adopted, avoiding the use of PIR regulators. The current harmonic distortion is accepted, and the harmonics in both current and back-emf are combined in a novel post-processing procedure to determine the $dq\theta$ flux maps. This permits the identification of higher order harmonics without the strict requirement of precisely controlling sinusoidal currents during data collection.

II. SyRM Model with Spatial Harmonics

This section introduces the notation adopted for the $dq\theta$ flux maps modeling of SyRM. In particular, 2D vector quantities are written as lowercase **bold** symbols, while the matrices are represented with uppercase **bold** letters. Stationary and rotating reference frames are indicated as $\alpha\beta$ and dq, where the d-axis is the direction of maximum inductance.

The voltage equation of a synchronous machine can be expressed in the dq rotor reference frame:

$$\frac{\mathrm{d}\boldsymbol{\lambda}_{dq}}{\mathrm{d}t} = \boldsymbol{v}_{dq} - R_s \boldsymbol{i}_{dq} - \omega\, \mathbf{J}\, \boldsymbol{\lambda}_{dq} \tag{1}$$

where $\boldsymbol{\lambda}_{dq}(i_d, i_q, \theta)$ is the stator flux linkage vector, function of stator currents i_d, i_q and rotor position θ.

The flux derivative can be expressed using the incremental inductances:

$$\frac{\mathrm{d}\boldsymbol{\lambda}_{dq}}{\mathrm{d}t}(i_d, i_q, \theta) = \boldsymbol{L}_\partial \cdot \frac{\mathrm{d}\boldsymbol{i}_{dq}}{\mathrm{d}t} + \frac{\partial \boldsymbol{\lambda}_{dq}}{\partial \theta} \cdot \frac{\mathrm{d}\theta}{\mathrm{d}t} \tag{2}$$

where the incremental inductance matrix $\boldsymbol{L}_\partial$ is defined as:

$$\boldsymbol{L}_\partial(i_d, i_q, \theta) = \frac{\partial \boldsymbol{\lambda}_{dq}}{\partial \boldsymbol{i}_{dq}} = \begin{bmatrix} l_d & l_{dq} \\ l_{dq} & l_q \end{bmatrix} \tag{3}$$

where l_d, l_q and l_{dq} are the incremental inductances along d and q axes and the cross-saturation term, respectively. As graphically depicted in Figure 1, the flux-linkage vector, including the spatial harmonics effects, is expressed as:

$$\boldsymbol{\lambda}_{dq}(i_d, i_q, \theta) = \boldsymbol{L}\, \boldsymbol{i}_{dq} \tag{4}$$

$$\boldsymbol{L}(i_d, i_q, \theta) = \begin{bmatrix} L_d & 0 \\ 0 & L_q \end{bmatrix} \tag{5}$$

where L_d, L_q are the apparent inductances in d and q axes respectively, including the effects of self- and cross-saturation

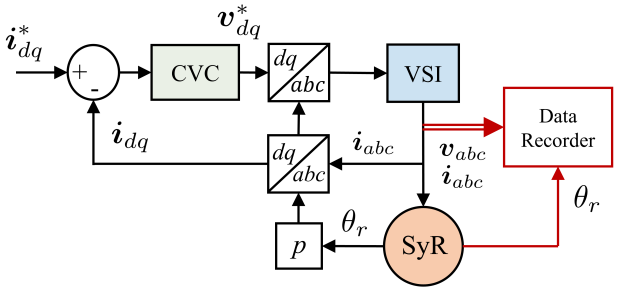

Fig. 2. Block diagram of the proposed commissioning for spatial flux linkage identification using PI Current Vector Control (CVC).

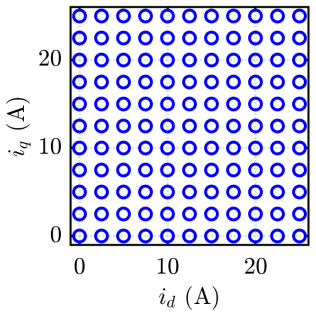

(a)

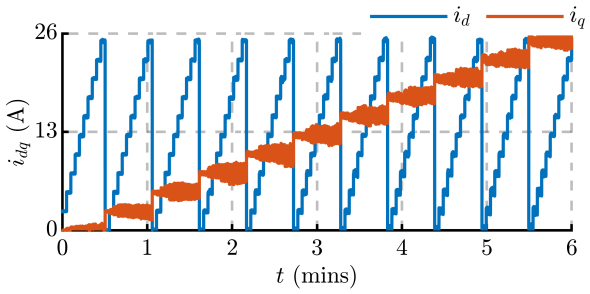

(b)

Fig. 3. (a) Regular grid of tested points in the dq current plane. (b) dq current trajectories during the identification test.

and the space harmonics. All the apparent and incremental inductances are functions of the three state variables: i_d, i_q and θ.

In the dq frame, the existing harmonics are multiples of $6n$, where n is an integer. Therefore, the magnetic model can be expressed by its Fourier series, only including the harmonics multiple of 6:

$$L_d(i_d, i_q, \theta) = L_{d0}(i_d, i_q) + \sum_{h=6n} L_{dh}(i_d, i_q)\, \cos(h\theta - \phi_{dh}) \tag{7a}$$

$$L_q(i_d, i_q, \theta) = L_{q0}(i_d, i_q) + \sum_{h=6n} L_{qh}(i_d, i_q)\, \cos(h\theta - \phi_{qh}) \tag{7b}$$

where L_{d0}, L_{q0} are the fundamental inductances, L_{dh}, L_{qh} are the inductance harmonic components magnitude, ϕ_{dh}, ϕ_{qh} are the inductance harmonic components phase angle and h is the harmonic order.

$$\boldsymbol{I}_d = \frac{1}{2}\begin{bmatrix} 2i_{d0} & i_{d6}\cos(\phi^i_{d6}) & i_{d6}\sin(\phi^i_{d6}) & i_{d12}\cos(\phi^i_{d12}) & i_{d12}\sin(\phi^i_{d12}) \\ 2i_{d6}\cos(\phi^i_{d6}) & 2i_{d0}+i_{d12}\cos(\phi^i_{d12}) & i_{d12}\sin(\phi^i_{d12}) & i_{d6}\cos(\phi^i_{d6}) & i_{d6}\sin(\phi^i_{d6}) \\ 2i_{d6}\sin(\phi^i_{d6}) & i_{d12}\sin(\phi^i_{d12}) & 2i_{d0}-i_{d12}\cos(\phi^i_{d12}) & -i_{d6}\sin(\phi^i_{d6}) & i_{d6}\cos(\phi^i_{d6}) \\ 2i_{d12}\cos(\phi^i_{d12}) & i_{d6}\cos(\phi^i_{d6}) & -i_{d6}\sin(\phi^i_{d6}) & 2i_{d0} & 0 \\ 2i_{d12}\sin(\phi^i_{d12}) & i_{d6}\sin(\phi^i_{d6}) & i_{d6}\cos(\phi^i_{d6}) & 0 & 2i_{d0} \end{bmatrix} \tag{6a}$$

$$\boldsymbol{L}_d = \begin{bmatrix} L_{d0} & L_{d6}\cos(\phi_{d6}) & L_{d6}\sin(\phi_{d6}) & L_{d12}\cos(\phi_{d12}) & L_{d12}\sin(\phi_{d12}) \end{bmatrix} \tag{6b}$$

$$\boldsymbol{\Lambda}_d = \begin{bmatrix} \lambda_{d0} & \lambda_{d6}\cos(\phi^\lambda_{d6}) & \lambda_{d6}\sin(\phi^\lambda_{d6}) & \lambda_{d12}\cos(\phi^\lambda_{d12}) & \lambda_{d12}\sin(\phi^\lambda_{d12}) \end{bmatrix} \tag{6c}$$

III. Proposed Space Harmonics Flux Identification Test

The block diagram of the control system is shown in Figure II. The motor under test (MUT) is closed loop current controlled while driven at a constant speed by a dyno drive. The current vector reference for the MUT control is set for systematically exploring a grid of points in the dq current plane, as depicted in . Each point under test in the dq current plane is maintained for at least one mechanical revolution. The current trajectories during the experimental identification are shown in Figure 3b.

In similar methods, such as [19], multiple resonant controllers eliminate the current harmonics, thus obtaining sinusoidal phase current and shifting all the harmonic information in the back-emf. However, this requires prior knowledge of the dominant harmonics which is not readily available for commercial off-the-shelf motors. Besides, the maximum harmonic order of the PIR controllers is limited by the operating speed and sampling frequency. Instead, the use of PI controller is simple and straightforward, but it scatters the harmonic information to both current and back-emf waveforms, depending on the harmonic order and the current controller bandwidth. This is illustrated in Figure III-A, showing the measured currents and the estimated fluxes of a single data-point. The dominant 12^{th} harmonic is poorly regulated due to the limited current controller bandwidth. Nevertheless, the proposed post-processing method is capable of merging the harmonic information from the current and flux waveforms, retrieving the spatial inductances and thus the $dq\theta$ flux-maps.

A. Data Post-Processing

Based on the voltage and current measurements, the stator flux is estimated in the stationary $\alpha\beta$ frame:

$$\boldsymbol{\lambda}_{\alpha\beta} = \int (\boldsymbol{v}_{\alpha\beta} - R_s\, \boldsymbol{i}_{\alpha\beta})\, \mathrm{d}t. \tag{8}$$

For each reference point of the test grid $\boldsymbol{i}^*_{dq}$, the current and flux harmonics are extracted using the Fourier transform:

$$i_d(i^*_d, i^*_q, \theta) = i_{d0}(i^*_d, i^*_q) + \sum_{h=6n} i_{dh}(i^*_d, i^*_q)\cos(h\theta - \phi^i_{dh}) \tag{9a}$$

$$i_q(i^*_d, i^*_q, \theta) = i_{q0}(i^*_d, i^*_q) + \sum_{h=6n} i_{qh}(i^*_d, i^*_q)\cos(h\theta - \phi^i_{qh}) \tag{9b}$$

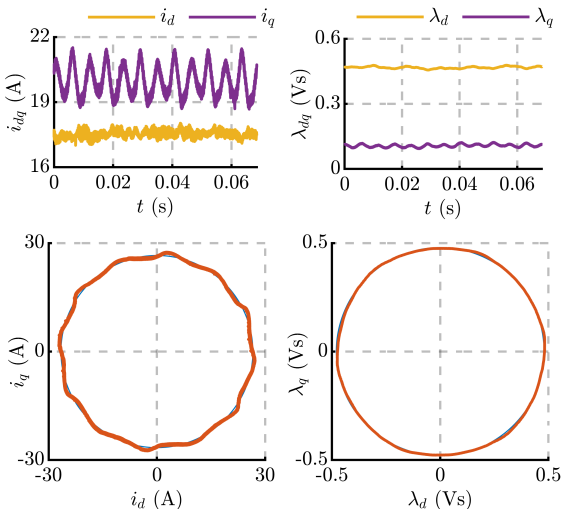

Fig. 4. Experimental examination of the harmonics (one electrical cycle) in the measured currents and estimated fluxes at a single data-point.

$$\lambda_d(i^*_d, i^*_q, \theta) = \lambda_{d0}(i^*_d, i^*_q) + \sum_{h=6n} \lambda_{dh}(i^*_d, i^*_q)\cos(h\theta - \phi^\lambda_{dh}) \tag{10a}$$

$$\lambda_q(i^*_d, i^*_q, \theta) = \lambda_{q0}(i^*_d, i^*_q) + \sum_{h=6n} \lambda_{qh}(i^*_d, i^*_q)\cos(h\theta - \phi^\lambda_{qh}) \tag{10b}$$

where $i_{d0} = i^*_d$, $i_{q0} = i^*_q$, λ_{d0}, λ_{q0} are the fundamental components of currents and fluxes, i_{dh}, i_{qh}, λ_{dh}, λ_{qh} are the harmonic components magnitudes and ϕ^i_{dh}, ϕ^i_{qh}, ϕ^λ_{dh}, ϕ^λ_{qh} are the harmonic components phase angles. The harmonics of λ_d in (10) are decomposed into sine and cosine components, i.e. $\lambda_{dh}\cos(\phi^\lambda_{dh})$ and $\lambda_{dh}\sin(\phi^\lambda_{dh})$, for ease of identification. This can be represented as the resulting interaction between the harmonic currents in (9), $i_{dh}\cos(\phi^i_{dh})$ and $i_{dh}\sin(\phi^i_{dh})$, and the harmonic inductances in (7), $L_{dh}\cos(\phi_{dh})$ and $L_{dh}\sin(\phi_{dh})$ as

$$\boldsymbol{\Lambda}_d = \boldsymbol{I}_d\, \boldsymbol{L}_d \tag{11}$$

where $\boldsymbol{\Lambda}_d$ and $\boldsymbol{L}_d$ are column vector matrices and $\boldsymbol{I}_d$ is a square matrix, reported in (6). For brevity, only the 6^{th} and 12^{th} harmonics are considered but the approach can be easily extended for higher orders.

The coefficient of the current harmonic matrix $\boldsymbol{I}_d$ and flux harmonic vector $\boldsymbol{\Lambda}_d$ are retrieved from the measured current

TABLE I
MOTOR PARAMETERS

Parameters	Symbol	Values	Units
Rated power	P_n	4.4	kW
Rated voltage	V_n	400	V
Rated speed	ω_n	2500	rpm
Rated current (pk)	I_n	15	A
Rated torque	T_n	17	Nm
Rated flux	λ_n	0.3	Vs
Pole pairs	p	3	-
Stator resistance	R_s	0.4	Ω

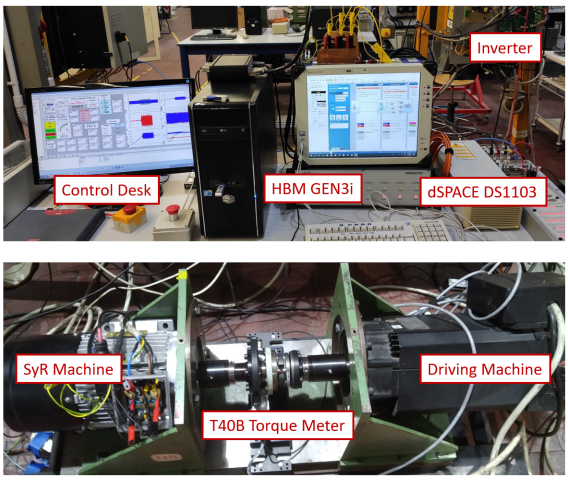

Fig. 5. Experimental setup, including the 4.4 kW SyRM under test, the dyno drive, the data recorder and the dSPACE DS1103 control platform.

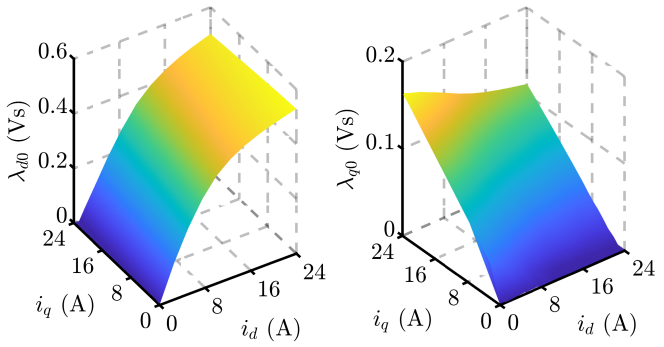

Fig. 6. Experimentally identified fundamental dq flux linkage maps of the SyRM under test.

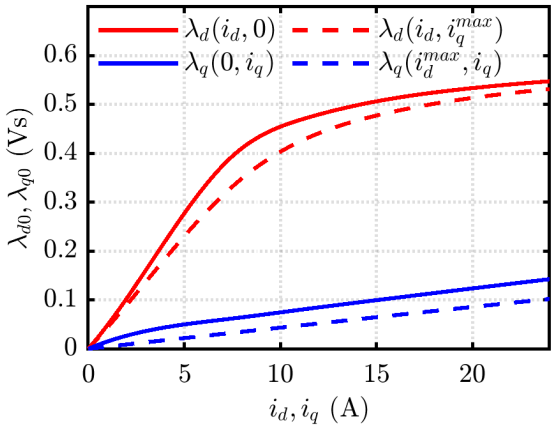

Fig. 7. Experimentally identified fundamental dq flux linkages of the SyRM under test: effect of the saturation and cross-saturation.

and the flux vector estimated by (8). Once $\boldsymbol{I}_d$ and $\boldsymbol{\Lambda}_d$ are determined, the inductance matrice $\boldsymbol{L}_d(i_d^*, i_q^*)$, summarizing the harmonic information of the flux maps, is computed for each tested point in the dq current grid (see Figure 3b).

$$\boldsymbol{L}_d = \boldsymbol{I}_d^{-1}\,\boldsymbol{\Lambda}_d \tag{12}$$

Similar equations (11),(6), not reported for brevity, apply for the q-axis, thus permitting to compute the harmonic inductance matrix $\boldsymbol{L}_q(i_d^*, i_q^*)$ for each tested point in the dq plane,

$$\boldsymbol{L}_q = \boldsymbol{I}_q^{-1}\,\boldsymbol{\Lambda}_q \tag{13}$$

To sum up: the proposed test sequence permits computing the harmonic components of the inductance matrices $\boldsymbol{L}_d, \boldsymbol{L}_q$ for each point of the dq plane. Based on these inductance matrices, the stator flux vector can be computed through (4),(5) as a function of i_d, i_q and θ.

IV. EXPERIMENTAL VALIDATION

The proposed flux harmonic identification technique is validated experimentally on a 4.4 kW SyRM with a rated current of 15 A and a rated torque of 17 Nm. The full motor parameters are tabulated in Table I, while the experimental setup is shown in Figure 5, depicting the motor under test, the dyno drive, the dSpace control platform and the data logger.

The fundamental flux maps are identified with the procedure presented in [8]: the motor under test (bottom left in Figure 5 is supplied with a custom inverter and current-controlled with a dSPACE DS1103 board (top right of Figure 5), following all the points on a regular grid on the (i_d, i_q) domain reported in Figure 3a. The MUT is coupled to a driving machine having torque and power ratings much higher than the MUT and shown in the bottom right of Figure 5. The driving machine is speed-controlled to maintain a constant rotor speed.

Dealing with the acquisition system, a high-speed data logger from HBM is adopted, allowing to record at 2 MHz. Both electrical and mechanical quantities are measures: phase currents are sampled through Ultrastab LEM sensors and line voltages are directly sampled from the HBM acquisition card. A T40B torque meter from HBM allows to measure directly torque and rotor position, enabling the accurate characterization of the MUT. The acquisition systems is operated in multi-sweeps mode: just the required measurement windows are recorded at high sampling frequency, while the transitions between the measurement points are not saved.

The dq current plane is explored in a regular grid up to

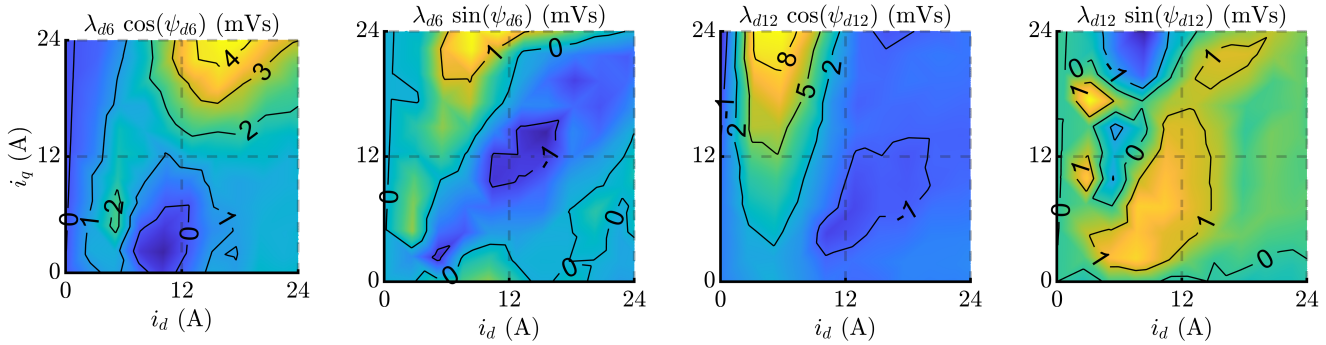

(a)

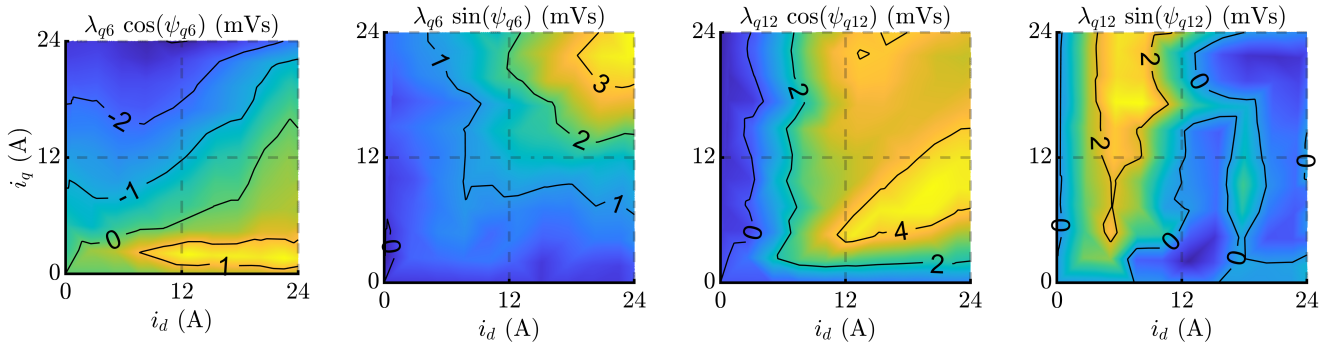

(b)

Fig. 8. Experimentally identified 6^{th} and 12^{th} harmonic components (sine and cosine) flux linkage of the 4.4 kW SyRM under test. (a) d-axis flux; (b) q-axis flux.

25 A, corresponding to 60% overload, in steps of 2.5A, as shown in Figures 3a and 3b, with the dyno drive imposing a constant speed of 300 rpm. The flux-linkage map is identified using (11). Figure 6 shows the measured fundamental dq flux estimates, λ_{d0} and λ_{q0}, as surfaces function of the dq currents. The saturation and cross saturation effects are more visible in Figure 7, where the flux linkage curves are reported function of the respective currents (red for d axis and blue for q axis), with zero current on the other axis (solid lines) and with the maximum current on the other axis (dashed lines). These are typical characteristic from SyRM and it is worth noting that at rated current the d axis flux linkage is saturated.

The contour plots of sine and cosine components of the 6^{th} and the 12^{th} harmonics are shown in Figures 8a and 8b for the d and q axes, respectively, where the dominance of the 12^{th} harmonic is observed. The maximum amplitude of the 6^{th} and the 12^{th} harmonics for the d-axis are 0.014 p.u. and 0.031 p.u. respectively, and for the q-axis are 0.008 p.u. and 0.015 p.u., respectively.

V. Conclusion

An experimental method for flux map identification of synchronous reluctance motors including its spatial harmonics is proposed. The dq current plane is systematically explored, and the harmonic information embedded in the acquired currents and back-emf is extracted to build the 3D $dq\theta$ flux-map as functions of stator currents and rotor position. By combining the ripple information in the measured current and emf, the proposed method permits to evaluate the flux space harmonic without the requirement of accurate sinusoidal control during the identification stage, thus considerably simplifying the testing sequence and procedure.

The proposed method benefits from simplicity and generality: in this work only 6^{th} and 12^{th} harmonics are considered for brevity but the procedure can be easily extended to higher order harmonics. A 4.4 kW SyRM is experimentally identified according to the proposed method, demonstrating the feasibility and the high accuracy of the proposed method for 3D flux map and spatial harmonics identification.

Acknowledgment

The research has been conducted with the support of Power Electronics Innovation Center (PEIC) of Politecnico di Torino.

References

[1] H. A. A. Awan, Z. Song, S. E. Saarakkala, and M. Hinkkanen, "Optimal Torque Control of Saturated Synchronous Motors: Plug-and-Play Method," *IEEE Trans. on Ind. Appl.*, 2018.

[2] A. G. Yepes, W. E. Abdel-Azim, A. Shawier, A. S. Abdel-Khalik, M. S. Hamad, S. Ahmed, and J. Doval-Gandoy, "Open-phase-tolerant online current references for maximum torque range and minimum loss with current and torque-ripple limits for n-phase nonsalient pmsms with nonsinusoidal back-emf," *IEEE Transactions on Transportation Electrification*, pp. 1–1, 2023.

[3] A. Yousefi-Talouki, F. Stella, S. Odhano, L. de Lilo, A. Trentin, G. Pellegrino, and P. Zanchetta, "Sensorless control of matrix converter-fed synchronous reluctance motor drives," in *2017 IEEE International Symposium on Sensorless Control for Electrical Drives (SLED)*, 2017, pp. 181–186.

[4] M. Tursini, M. Villani, G. Fabri, S. Paolini, A. Credo, and A. Fioravanti, "Sensorless control of a synchronous reluctance motor by finite elements model results," in *2017 IEEE International Symposium on Sensorless Control for Electrical Drives (SLED)*, 2017, pp. 19–24.

[5] F. J. W. Barnard, W. T. Villet, and M. J. Kamper, "Hybrid active-flux and arbitrary injection position sensorless control of reluctance synchronous machines," *IEEE Transactions on Industry Applications*, vol. 51, no. 5, pp. 3899–3906, 2015.

[6] S.-C. Agarlita, I. Boldea, and F. Blaabjerg, "High-frequency-injection-assisted "active-flux"-based sensorless vector control of reluctance synchronous motors, with experiments from zero speed," *IEEE Transactions on Industry Applications*, vol. 48, no. 6, pp. 1931–1939, 2012.

[7] A. Varatharajan, D. Brunelli, S. Ferrari, P. Pescetto, and G. Pellegrino, "syredrive: Automated sensorless control code generation for synchronous reluctance motor drives," in *2021 IEEE Workshop on Electrical Machines Design, Control and Diagnosis (WEMDCD)*, 2021, pp. 192–197.

[8] E. Armando, R. I. Bojoi, P. Guglielmi, G. Pellegrino, and M. Pastorelli, "Experimental identification of the magnetic model of synchronous machines," *IEEE Transactions on Industry Applications*, vol. 49, no. 5, pp. 2116–2125, 2013.

[9] IEEE, "IEEE Trial-Use Guide for Testing Permanent Magnet Machines," pp. 1–56, 2015.

[10] N. Bedetti, S. Calligaro, and R. Petrella, "Stand-Still Self-Identification of Flux Characteristics for Synchronous Reluctance Machines Using Novel Saturation Approximating Function and Multiple Linear Regression," *IEEE Transactions on Industry Applications*, 2016.

[11] A. Varatharajan, P. Pescetto, and G. Pellegrino, "Sensorless self-commissioning of synchronous reluctance machine with rotor self-locking mechanism," in *2019 IEEE Energy Conversion Congress and Exposition (ECCE)*, 2019, pp. 812–817.

[12] L. Ortombina, D. Pasqualotto, F. Tinazzi, and M. Zigliotto, "Magnetic model identification for synchronous reluctance motors including transients," in *2019 IEEE Energy Conversion Congress and Exposition (ECCE)*, 2019, pp. 3196–3202.

[13] P. Pescetto and G. Pellegrino, "Determination of pm flux linkage based on minimum saliency tracking for pm-syr machines without rotor movement," *IEEE Transactions on Industry Applications*, vol. 56, no. 5, pp. 4924–4933, 2020.

[14] I. Hwang, Y.-C. Kwon, and S.-K. Sul, "Enhanced dynamic operation of heavily saturated ipmsm in signal-injection sensorless control with ancillary reference frame," *IEEE Transactions on Power Electronics*, vol. 38, no. 5, pp. 5726–5741, 2023.

[15] R. Leuzzi, P. Cagnetta, S. Ferrari, P. Pescetto, G. Pellegrino, and F. Cupertino, "Transient overload characteristics of pm-assisted synchronous reluctance machines, including sensorless control feasibility," *IEEE Transactions on Industry Applications*, vol. 55, no. 3, pp. 2637–2648, 2019.

[16] S. Foti, S. De Caro, T. Scimone, A. Testa, L. D. Tornello, G. Scelba, and M. Cacciato, "Rotor position error compensation in sensorless synchronous reluctance motor drives," *IEEE Transactions on Power Electronics*, vol. 37, no. 4, pp. 4442–4452, 2022.

[17] F. Stella, A. Yousefi-Talouki, S. Odhano, G. Pellegrino, and P. Zanchetta, "An accurate self-commissioning technique for matrix converters applied to sensorless control of synchronous reluctance motor drives," *IEEE Journal of Emerging and Selected Topics in Power Electronics*, vol. 7, no. 2, pp. 1342–1351, 2019.

[18] S. Ferrari, G. Dilevrano, P. Ragazzo, and G. Pellegrino, "The dq-theta Flux Map Model of Synchronous Machines," in *IEEE Energy Conversion Congress and Exposition (ECCE)*, 2021.

[19] J. Lee, Y. C. Kwon, and S. K. Sul, "Identification of IPMSM Flux-Linkage Map for High-Accuracy Simulation of IPMSM Drives," *IEEE Transactions on Power Electronics*, 2021.

[20] X. Chen, J. Wang, B. Sen, P. Lazari, and T. Sun, "A high-fidelity and computationally efficient model for interior permanent-magnet machines considering the magnetic saturation, spatial harmonics, and iron loss effect," *IEEE Transactions on Industrial Electronics*, vol. 62, no. 7, pp. 4044–4055, 2015.